Energy Storage Materials 40 (2021) 386–393

Contents lists available at ScienceDirect

Energy Storage Materials

journal homepage: www.elsevier.com/locate/ensm

Identifying descriptors for Li^+ conduction in cubic Li-argyrodites *via* hierarchically encoding crystal structure and inferring causality

Qian Zhao [a], Liwen Zhang [b], Bing He [c], Anjiang Ye [c], Maxim Avdeev [d,e], Liquan Chen [a,f], Siqi Shi [a,b,*]

[a] Materials Genome Institute, Shanghai University, Shanghai 200444, China
[b] School of Materials Science and Engineering, Shanghai University, Shanghai 200444, China
[c] School of Computer Engineering and Science, Shanghai University, Shanghai 200444, China
[d] Australian Nuclear Science and Technology Organization, New Illawarra Rd, Lucas Heights, NSW 2234, Australia
[e] School of Chemistry, The University of Sydney, Sydney 2006, Australia
[f] Key Laboratory for Renewable Energy, Institute of Physics, Chinese Academy of Sciences, Beijing 100190, China

ARTICLE INFO

Keywords:
Descriptors
Li^+ conduction
Solid state electrolytes (SSEs)
Li-argyrodites

ABSTRACT

Identifying descriptors linked to Li^+ conduction enables rational design of solid state electrolytes (SSEs) for advanced lithium ion batteries, but it is hindered by the diverse and confounding descriptors. To address this, by integrating global and local effects of Li^+ conduction environment, we develop a generic method of hierarchically encoding crystal structure (HECS) and inferring causality to identify descriptors for Li^+ conduction in SSEs. Taking the cubic Li-argyrodites as an example, 32 HECS-descriptors are constructed, encompassing composition, structure, conduction pathway, ion distribution, and special ions derived from the unit cell information. Partial correlation analysis reveals that the smaller anion size plays a significant role in achieving lower activation energy, which results from the competing effects between the lattice space and bottleneck size controlled by framework site disorder. Moreover, the promising candidates are suggested, in which $Li_{6-x}PS_{5-x}Cl_{1+x}$ (*e.g.*, $Li_{5.5}PS_{4.5}Cl_{1.5}$ with the room ionic conductivity of 9.4mS cm^{-1} and the activation energy of 0.29eV) have been experimentally evaluated as excellent candidates for practical SSEs and the rest are novel compositions waiting for validation. Our work establishes a rational correlation between the HECS-descriptors and Li^+ conduction and the proposed approach can be extended to other types of SSE materials.

1. Introduction

Over the past few decades, solid state electrolytes (SSEs) have garnered considerable attention due to their potential for the realization of safer and more reliable batteries with higher energy and power densities [1-7]. A large number of inorganic materials including LiSICON-like (lithium superionic conductor) [8], lithium nitrides [9], lithium halides [10], garnets [11], NaSICON-like (sodium superionic conductor) [12], argyrodites [13], and lithium hydrides [14], with both crystalline and amorphous structures as well as their composite structures have been explored theoretically and experimentally as potential SSEs candidates, in parallel to very active search for new SSEs with high ionic conductivity and low activation energy (E_a). To accelerate this search process, one promising strategy is to undertake rational material design by identifying appropriate material descriptors linked to ion conduction in SSEs.

Several descriptors related to ion conduction have been proposed previously. For example, Wakamura correlated optical phonon frequencies with E_a and proposed that low-energy optical (LEO) phonon can assist the conduction of mobile ions in selected classes of materials [15]. Yang Shao-Horn's group related the lattice volume and conduction bottleneck size to lithium-ion conductivity across several well-known structural families and proposed that the increasing lattice volume and lithium-ion diffusion bottleneck size can increase the ionic conductivity and reduce E_a for these structural families [16]. Zhao et al. correlated polyanion rotation with ionic conductivity and elucidated increasing lattice volume can cause the unexpected lowering of the ionic conductivity in inorganic plastic crystal electrolytes [17]. Wang *et al.* correlated the anion sublattice topology with ionic conduction and demonstrated that the bcc-like topology benefits higher ion mobility [18]. Additionally, the collective role of several descriptors was also highlighted, *e.g.* Fujimura *et al.* correlated diffusion coefficients at 1600K, D_{1600}, transition temperature, T_c, formation free energies of solid solution formation at 1600K, $\Delta F^S{}_{1600}$, and average volume of disordered structures, V_{dis}, with chemical composition for rational design of superior Li-ion conductors through machine-learning techniques [19]. Sendek *et al.* established 20 atomistic descriptors for several systems and defined a

* Corresponding author at: Shanghai University, 333 Nanchen Road, Shanghai 200444, China.
E-mail address: sqshi@shu.edu.cn (S. Shi).

https://doi.org/10.1016/j.ensm.2021.05.033
Received 7 February 2021; Received in revised form 24 April 2021; Accepted 23 May 2021
Available online 29 May 2021

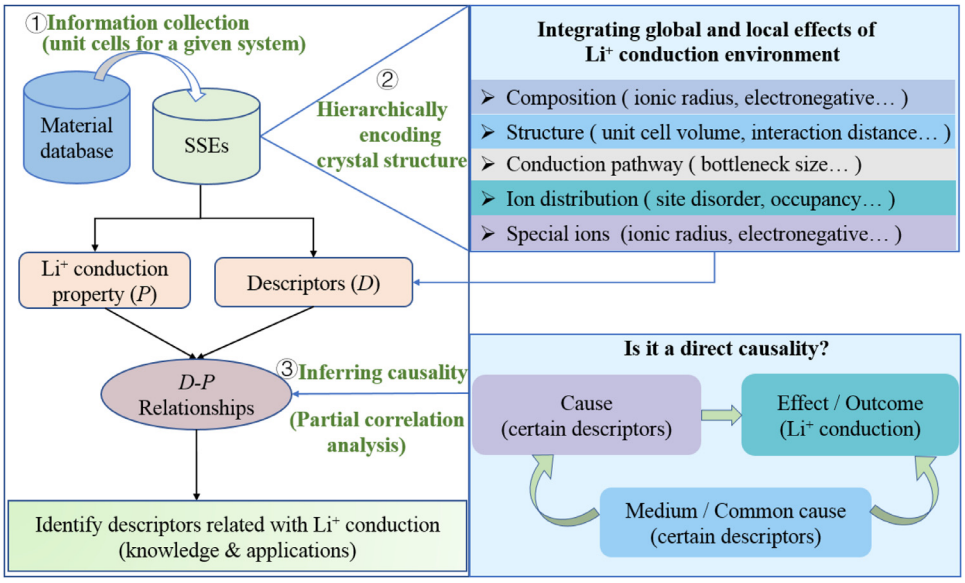

Fig. 1. Schematic representation of the methodology for identifying descriptors for Li^+ conduction in solid state electrolytes.

multi-descriptor model capable of predicting superionic behavior and automatically probing complex mutual correlations by machine learning [20]. It is noted that descriptors related to ion conduction are of both diversity and particularity and sometimes some counterfactuals and interventions exist, which originate from the varying and complex ion conduction mechanisms in diverse SSEs. Inspired by this, we aim to propose a simple and generic approach to identify descriptors for Li^+ conduction in SSEs. Here, by incorporating global and local effects of Li^+ conduction environment, we develop the generic hierarchically encoding crystal structure-based (HECS) descriptors encompassing composition, structure, conduction pathway, ion distribution, and special ions derived from the unit cell information. Then their causalities with Li^+ conduction property are inferred *via* partial correlation analysis, which allows exploration of counterfactuals and interventions and avoids correlative but incorrect conclusions. Fig. 1 shows the schematic of this methodology. And we take Li-argyrodites, one of the large families of SSEs, as an example to elaborate on it.

Li-argyrodite-type compounds are promising candidates as SSEs for lithium batteries due to the high Li^+ mobility and lithium content. Despite the increasing amount of relevant research, the general rules governing the ionic conduction have not yet been fully understood. Most of argyrodites crystallize in the form of cubic $F\bar{4}3m$ space group and exhibit similar framework topology and three-dimensional network of ion conduction pathways [21]. Moreover, numerous chemical substitutions were shown to change the lattice parameters and polarizability of their lattices without significantly changing the conduction pathways [22]. These special characteristics provide a scope for understanding the correlations between composition, local structure, and Li^+ conduction and make these materials an ideal model system. Therefore, in this paper, a systematic analysis on identifying descriptors for Li^+ conduction in these materials is conducted.

The paper is organized as follows. First, 50 eligible cubic Li-argyrodite compounds with the general formula $Li^+_{7-x+y}(M^{5+}_{1-y}N^{4+}_{y}Y(1)^{2-}_{4})Y(2)^{2-}_{2-x}X^{-}_{x}$ (M^{5+} = P^{5+}, As^{5+}; N^{4+}=Si^{4+}, Ge^{4+}, Sn^{4+}; Y^{2-}= S^{2-}, Se^{2-}; X^{-}= Cl^{-}, Br^{-}, I^{-}; $0\le x\le 2$, $0\le y\le 1$), are selected using our high-throughput screening platform for solid electrolytes (SPSE) [23] and their characteristics are systematically analyzed. Second, 32 HECS-descriptors are established and ion conduction property is quantified by E_a based on the potential energy landscape. Last, descriptors-E_a causalities are explored by partial correlation analysis. The design rules and promising compositions are identified, as described in detail below.

2. Methods and calculations

2.1. Activation energy calculations

To preserve the experimentally determined structure information and achieve high-efficiency calculation, E_a is uniformly calculated by the Bond-Valence Site Energy (BVSE) program embedded in the SPSE [23] instead of density functional theory (DFT) method, where BVSE is built upon the BV-based force-field approach proposed by Adams *et al.* [24]. E_a is calculated as a sum of the terms presenting the attraction between Li^+ and surrounding anions described by Morse-type potential and the repulsion between Li^+ and surrounding cations expressed by Coulombic potential as follows,

$$E(\mathrm{Li})_{\mathrm{morse}} = D_0/2\left\{\left(\exp\left[\alpha\left(R_{\min}-R\right)\right]-1\right)^2-1\right\} \quad (1)$$

$$E(\mathrm{Li}-A)_{\mathrm{Coulomb}} = \frac{q_{\mathrm{Li}}q_A}{R_{\mathrm{Li}-A}}\mathrm{erfc}\left(\frac{R_{\mathrm{Li}-A}}{\rho_{\mathrm{Li}-A}}\right) \quad (2)$$

where D_0, α and $R_{\min}$ are Morse potential parameters determined empirically and tabulated, q and R refer to effective charges of atoms and bond distance between the atoms, respectively. The use of $D_0/2$ instead of the original formulation with D_0 [25] is a simplified way to take into account relaxation in the immobile substructure and reach semiquantitative agreement with the migration barriers based on the available DFT or experimental information.

2.2. Multidimensional descriptors calculations

Structural information, such as lattice parameters, unit cell volume, interatomic distance, bond lengths and polyhedral volumes are extracted using the VESTA software (Version 3) [26]. Bottleneck size is calculated by the geometric analysis program CAVD (Crystal structure Analysis by Voronoi Decomposition [27]) developed by our group [28]. All ionic radii are from Shannon [29]. Cation or anion disorder stemming from the site mixing of ions in the individual sublattices is quantified by configurational entropy, S_{conf} [30], which is expressed via site occupancies as:

$$S_{\mathrm{conf}} = -\mathrm{R}\sum_j q_j \sum_i X_{ij}\ln X_{ij} \quad (3)$$

with q_j denoting the number of sites in the sublattice j, X_{ij} the mole fraction of the ion i on the j-th sublattice, the summation extending over all ions i on the j-th sublattice, and over all the sublattices j.

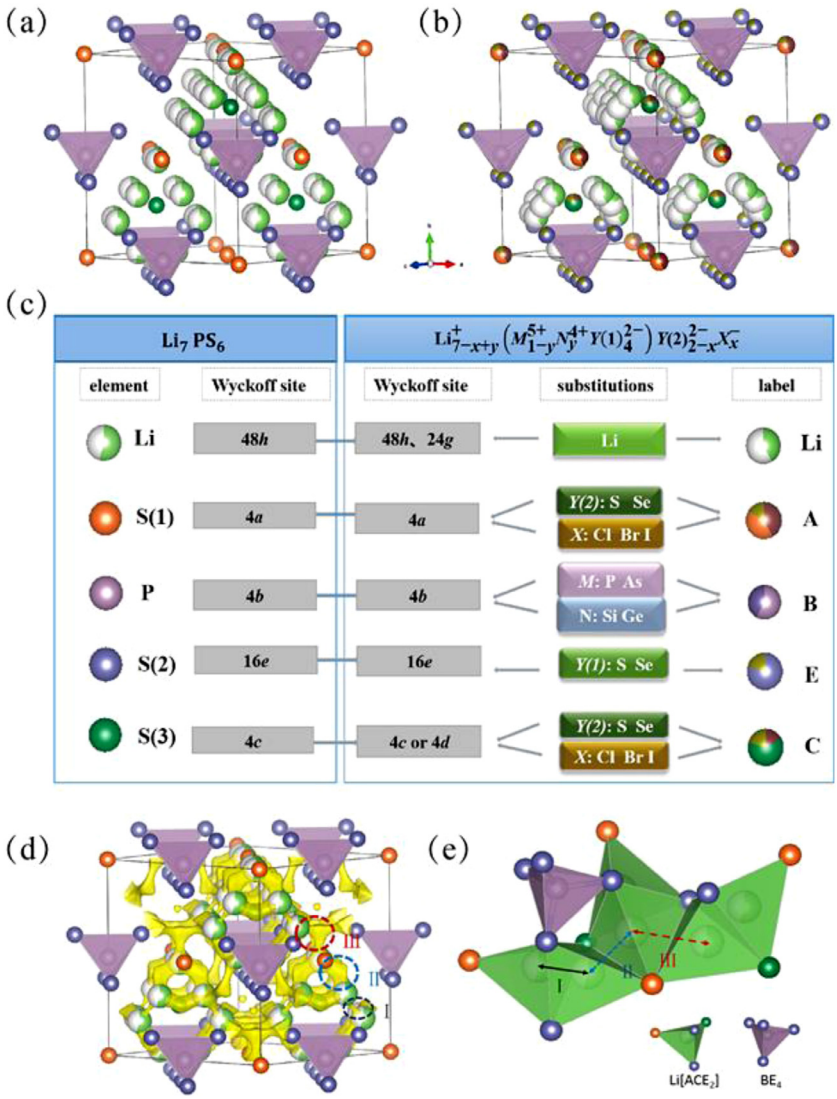

Fig. 2. Schematic crystal structure of (a) cubic Li_7PS_6 with F$\bar{4}$3m (No.216) space group and (b) cubic $Li^{+}_{7-x+y}(M^{5+}_{1-y}N^{4+}_{y}Y(1)^{2-}_{4})Y(2)^{2-}_{2-x}X^{-}_{x}$ (M^{5+} = P^{5+}, As^{5+}; N^{4+}=Si^{4+}, Ge^{4+}, Sn^{4+}; Y^{2-}= S^{2-}, Se^{2-}; X^{-}= Cl^{-}, Br^{-}, I^{-}; 0≤x≤2, 0≤y≤1) with F$\bar{4}$3m (No.216) space group; (c) substitutions and their corresponding Wyckoff sites; (d) conduction pathway for cubic Li-argyrodite compounds (taking Li_7PS_6 as an example). The Li positions form pseudo-octahedral cages in which multiple conduction processes are possible; (e) conduction pathway between the lithium positions: I) doublet conduction (48*h*–24*g*–48*h*), II) intra-cage conduction (48*h*–48*h*), and III) inter-cage conduction (48*h*–48*h*). The free $S(1)^{2-}$ (symbol A) and $S(3)^{2-}$ (symbol C) anions and the corner of the $PS(2)_4^{2-}$ tetrahedra form Frank–Kasper polyhedra Li [ACE_2], which encloses two different Li positions (Wyckoff 48*h* and 24*g*). The mixed site occupancy is indicated by mixed colors.

2.3. Partial correlation analysis

Descriptors governing ionic conduction in SSEs are intricate and unveiling their causal relationships is challenging. Partial correlation is a powerful tool to distinguish whether the correlation between two variables is due to the direct causal relationship between them or due to the intermediate variables (common cause), which is a step in the direction of causal inference to discover the associations in data and helps to reveal the essential rule. The order of the partial correlation is determined by the number of variables it is conditioned on.

When the number of control variables is zero, the partial correlation is called the zero-order partial correlation or correlation analysis, which is performed to analyze the correlation among variables and extract detailed information on them. The degree of correlation can be measured by Pearson correlation coefficient (r_p), which is defined as the covariance of two variables (x, y) divided by the product of their standard deviations, as follows:

$$r_p(x, y) = \frac{cov(x, y)}{\sqrt{var(x)var(y)}} \tag{4}$$

When the number of control variables is one, the partial correlation is called the first-order partial correlation, which is measured by the first-order partial correlation coefficient. For instance, $r_p(x,y.z)$ is a first-order partial correlation coefficient, which quantifies the correlation between x and y that are uncorrelated with z. The first-order correlation can be calculated by the following equation:

$$r_p(x, y.z) = \frac{r_p(x, y) - r_p(x, z)r_p(y, z)}{\sqrt{\left(1 - r^2_{p(x,z)}\right)\left(1 - r^2_{p(y,z)}\right)}} \tag{5}$$

Similar equations exist to calculate higher-order coefficients. First or higher order partial correlation analysis can identify indirect dependencies, that is, investigate how the correlation between two variables is a result of their correlation to a third variable.

The Python software packages SciPy [31], NumPy [32], matplotlib [33], and plotly [34] are used for computing Pearson correlation coefficients r_p and perform data visualization. Results are considered to be strongly correlated at 0.5<|r_p|<1.0, moderately correlated at 0.3<|r_p|<0.5, weakly correlated at 0.1<|r_p|<0.3, and uncorrelated at 0.0<|r_p|<0.1.

3. Results and discussions

3.1. Characteristics of cubic Li-argyrodite compounds

The 50 studied cubic Li-argyrodite compounds can be regarded as various anion/cation substituted derivatives of the cubic Li_7PS_6. Fig. 2a shows the unit cell of Li_7PS_6 with the F$\bar{4}$3m (No.216) space group. The

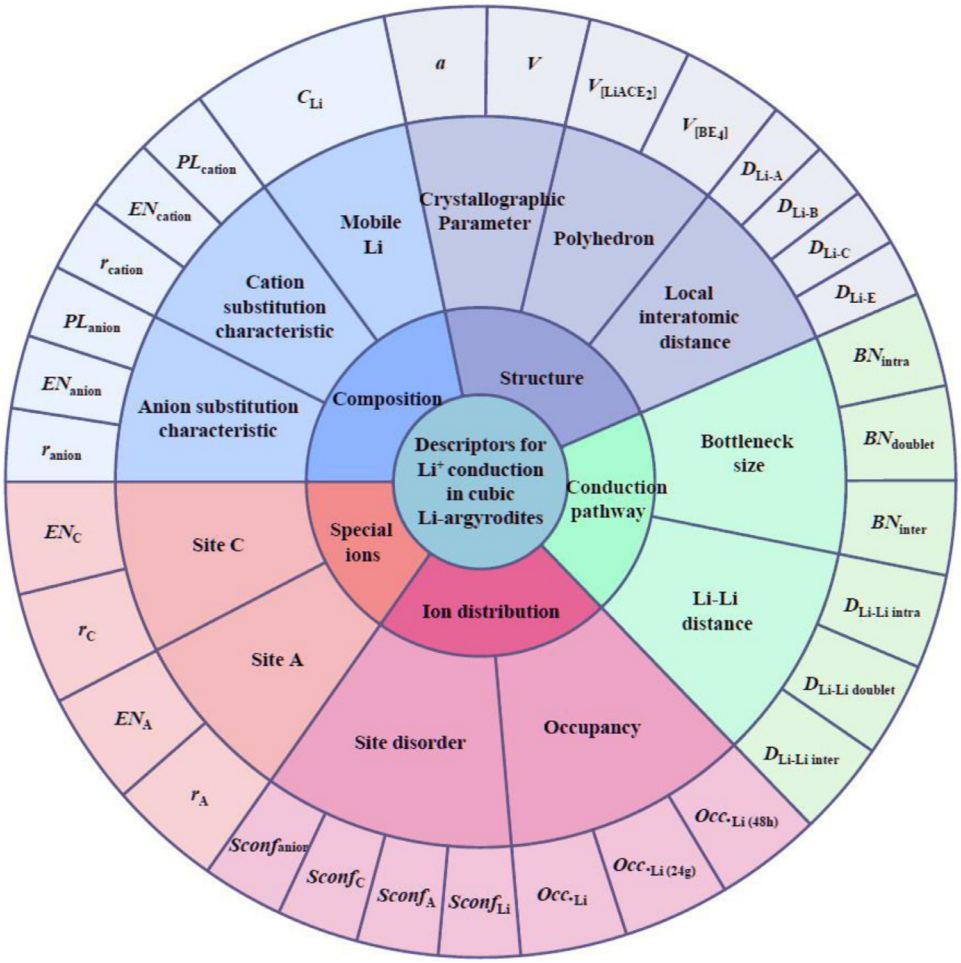

Fig. 3. HECS-descriptors for Li^+ conduction in cubic Li-argyrodite compounds.

$S(1)^{2-}$ (Wyckoff site 4*a*) form a face-centered cubic (FCC) close-packed lattice with $PS(2)_4^{3-}$ tetrahedra (formed by $S(2)^{2-}$ on the Wyckoff site 16*e* and P^{5+} on the Wyckoff site 4*b*) as the backbone and the free $S(3)^{2-}$ in half of the tetrahedral sites/voids on the Wyckoff site 4*c* (or 4*d* in alternative space group setting). The Li^+ are randomly distributed over the remaining tetrahedral cavities (Wyckoff site 48*h*), forming Li^+ cages around the free $S(3)^{2-}$ on the Wyckoff site 4*c*.

The argyrodites can be presented with the general formula $Li^+_{7-x+y}(M^{5+}_{1-y}N^{4+}_yY(1)^{2-}_4)Y(2)^{2-}_{2-x}X^-_x$ (M^{5+} = P^{5+}, As^{5+}; N^{4+}=Si^{4+}, Ge^{4+}, Sn^{4+}; Y^{2-}= S^{2-}, Se^{2-}; X^-= Cl^-, Br^-, I^-; $0\leq x\leq 2$, $0\leq y\leq 1$), which is characterized by a partial replacement of the S^{2-} with halogen ions (Cl^-,Br^-,I^-) or other chalcogen ions (Se^{2-}) and a substitution of As^{5+}, Si^{4+} or Ge^{4+} for P^{5+} (Fig. 2b and c). For realizing charge balance, the number of Li^+ changes accordingly. With increasing Li^+ content, Li^+ also occupy the Wyckoff 24g site. The two lithium positions (Wyckoff sites 48*h* and 24*g*) form cage-like local polyhedron, enabling three different conduction processes to occur during ionic conduction among neighboring lithium positions: I) doublet conduction (48*h*–24*g*–48*h*), II) intra-cage conduction (48*h*–48*h*), and III) inter-cage conduction (48*h*–48*h*), as shown in Fig. 2d and e.

All of the three conduction processes contribute towards the macroscopic Li^+ conduction in cubic Li-argyrodite compounds. Overall, all cubic phases of Li-argyrodites exhibit a three-dimensional network of Li^+ conduction pathways connecting partially occupied sites and hence show ionic conductivity.

E_a is the energy needed to realize Li-ion conduction. Table S1 shows the experimental E_a data available from literatures, some of which are missing and some of which are not unique. The available experimental E_a data are generally derived from the Arrhenius law and the values for the same compound differ with different experimental measurements. For instance, E_a determined from nuclear magnetic resonance (NMR) can be significantly smaller than that obtained from impedance spectroscopy, which can in part be due to the difficulties in decoupling the bulk and grain boundary contributions from the impedance data whereas NMR is bulk selective. Meantime, for impedance data, other factors, *e.g.*, differences in the electrode types and sample preparation conditions, can also influence the measured results. Therefore, for consistent comparison, the BVSE method is performed to assess the changes of ion conduction property across all the 50 studied compounds, and their corresponding E_a values are listed in Table S1.

3.2. Descriptors construction for Li^+ conduction in cubic Li-argyrodite compounds

For the 50 cubic Li-argyrodite compounds mentioned above, we hierarchically encode their crystal structure, involving composition, structure, conduction pathway, ion distribution, and special ions (Fig. 3).

The compositions are described in terms of the intrinsic properties of the elements, such as ionic radius (r_{cation}, r_{anion}), electronegativity (EN_{cation}, EN_{anion}), polarizability (PL_{cation}, PL_{anion}), and lithium content (C_{Li}). The structure is characterized in terms of its inherent parameters, such as lattice parameters (*a, a=b=c*), unit cell volume (*V*), the volume of polyhedra ($V_{[BE_4]^{3-}}$, $V_{[LiACE_2]^{3-}}$), as well as the distance between Li and surrounding ions ($D_{Li\text{-}A}$, $D_{Li\text{-}B}$, $D_{Li\text{-}C}$, $D_{Li\text{-}E}$). The conduction pathway is described based on the bottleneck size ($BN_{doublet}$, BN_{intra}, BN_{inter}) and the distance between the equilibrium Li^+ positions ($D_{Li\text{-}Li\ doublet}$, $D_{Li\text{-}Li\ intra}$, $D_{Li\text{-}Li\ inter}$). Since most of these compounds are not as well

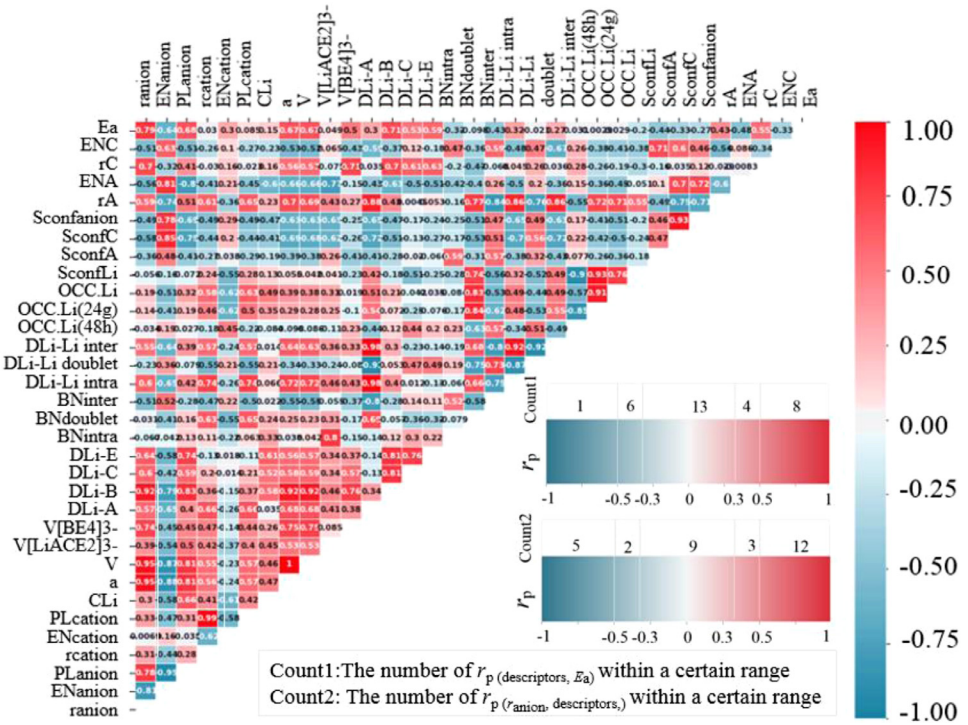

Fig. 4. Pearson correlation coefficient heatmap, illustrating the "descriptors-E_a" correlations and "descriptors-descriptors" relationships. The embedded subgraph in the lower right shows the number of $r_{p\ (descriptors,\ Ea)}$ and $r_{p\ (ranion,\ descriptors)}$ within a certain range respectively. Red and blue shades indicate positive and negative correlation between the two variables, respectively.

behaved as ideal crystals, the ionic disorder is quantified by the configurational entropy (*Sconf*) computed from the site occupancies for each sublattice using Eq 3, *i.e.* $Sconf_{Li}$, $Sconf_A$, $Sconf_C$, $Sconf_{anion}$, and Li sites occupancies ($Occ_{Li(48h)}$, $Occ_{Li(24g)}$, Occ_{Li}) are used as well. Lastly, the presence of special ions on Wyckoff 4*a* or 4*c* sites, *i.e.* outside and inside the Li^+ cages, respectively, may play a role in lithium conduction due to the changes in local structure. Therefore, r_A, r_C, EN_A, EN_C are used as descriptors to capture their radius and electronegativity. A full list of the total 32 HECS-descriptors accompanied with their definitions is presented in Table S2.

3.3. "*Descriptors*-E_a" causality inference in cubic Li-argyrodite compounds

32 HECS-descriptors presented in Fig. 3 and Table S2 are possible factors affecting the E_a of cubic Li-argyrodite electrolytes. A basic question arises as to whether 32 descriptors and E_a are correlated and, if so, whether they are direct causalities and what are the underlying physical mechanisms.

3.3.1. *Rules underlying the "descriptors-*E_a*" relationships*

Fig. 4 illustrates a Pearson correlation coefficient heatmap and the statistical number of $r_{p\ (descriptors,\ Ea)}$ and $r_{p\ (ranion,\ descriptors)}$ within a certain range respectively. There are 19 descriptors with absolute value of correlation coefficients ($|r_{p\ (descriptors,\ Ea)}|$) greater than 0.3 ($|r_p|>0.3$) and 9 of these is greater than 0.5, which indicates that these descriptors are possible robust design criteria for the cubic Li-argyrodite structure. The remaining 13 descriptors are weakly correlated with E_a but their impacts on E_a cannot be ruled out.

In particular, of these, r_{anion} has the strongest correlation with E_a and most descriptors are correlated with r_{anion}, which suggests the presence of common causal mechanisms across the overall cubic Li-argyrodites. It's likely that the effect of r_{anion} enables most descriptors to exhibit significant correlation with E_a. Previous studies [13,21,22,35-40] also separately elucidated the impact of anion substitutions on crystal structure and then Li^+ conduction. To test the hypothesis, we make first order partial correlation analysis on the "descriptors-E_a" correlation when conditioning on r_{anion}, which is a key step in the direction of causal inference. Fig. 5a demonstrates that the degree and direction of the correlation between descriptors and E_a clearly change after controlling r_{anion}. Therefore, the impact of these structure characteristics on Li^+ conduction is mainly induced by anion substitutions.

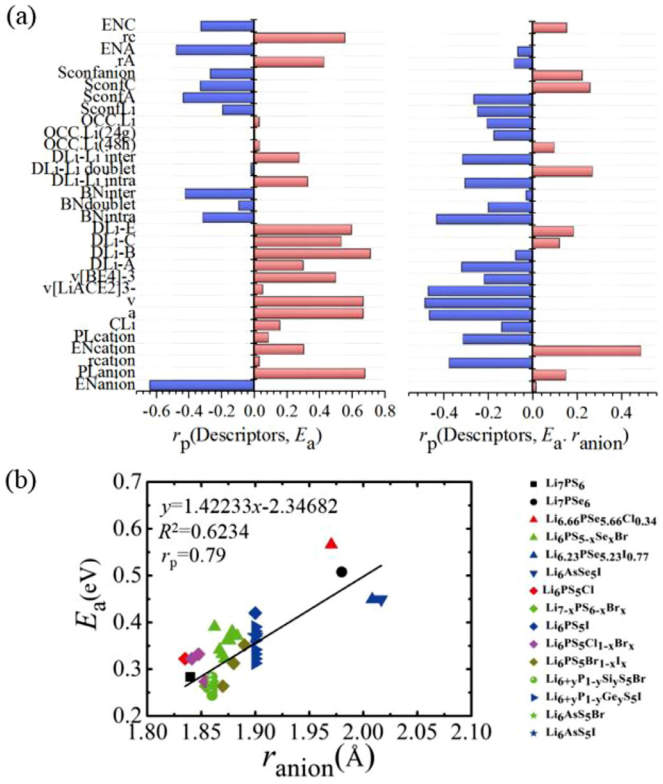

Fig. 5. (a) Comparison of "Descriptors-E_a" Pearson correlation coefficients obtained by correlation analysis (left) and partial correlation analysis under the condition of controlling r_{anion} (right). (b) Scatter diagram of r_{anion}-E_a correlation. The black straight line is the best linear regression fitting. Symbols of different colors and shapes indicate different compounds.

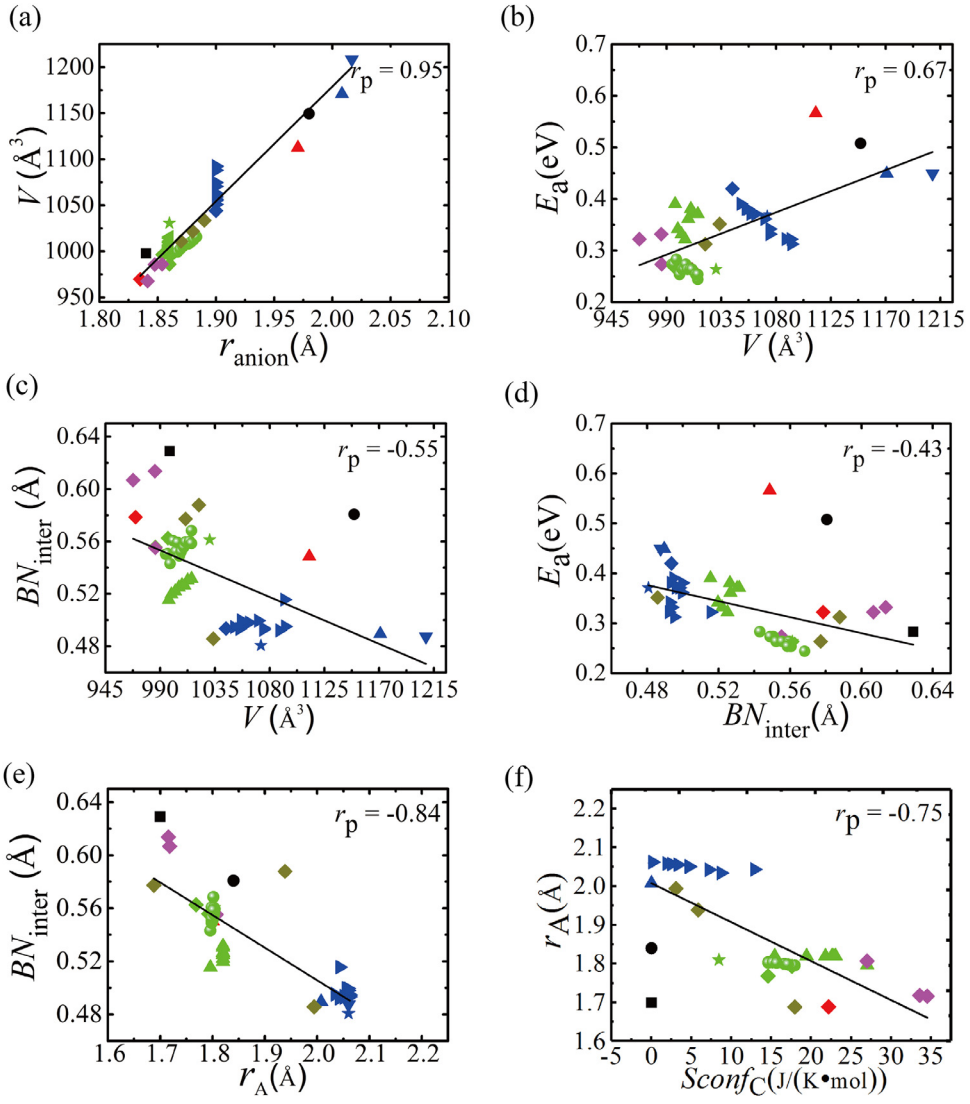

Fig. 6. Influence of (a) r_{anion} on unit cell volume v, (b) v on E_a, (c) v on BN_{inter}, (d) BN_{inter} on E_a, (e) r_A on BN_{inter}, and (f) $Sconf_C$ on r_A. The best-fit linear regression lines (black straight line) together with the Pearson correlation coefficients r_p (in the top-right corner) are displayed in each panel.

Fig. 5b shows the influence of r_{anion} on E_a. Due to the lack of data with r_{anion} ranging from 1.9 Å to 1.97 Å, two clusters of points exist and the points in the upper clusters have high leverage. Nevertheless, the overall trend originated from existing data clearly indicates that E_a increases with an increasing r_{anion}. It is concluded that anion substitutions with smaller (bigger) size give rise to lower (higher) E_a in the studied cubic Li-argyrodite materials. It is the first time to find this rule from the overall known cubic Li-argyrodites. Note that the size of substituting anion is avoided being too small to maintain the previous framework topology (e.g. oxide argyrodites Li_6PO_5X (X = Cl^-, Br^-)).

3.3.2. *Physical explanations on the "descriptors-E_a" relationship*

Identifying the common causal mechanisms can be used to untangle and simplify the complex correlations between 32 descriptors characterizing crystal structure and E_a. Fig. S1 shows the "r_{anion}-descriptors-E_a" correlation network, which illustrates the impact of anion substitutions on both the resultant structure and conduction property. r_{anion} demonstrates different degree of influence on multi-hierarchy descriptors. First, for the composition-derived descriptors, PL_{anion} and EN_{anion} are highly correlated with r_{anion}, as expected. Second, the correlation between r_{anion} and structure-derived descriptors is also consistent with the well-known empirical crystal chemical rules, *i.e.*, the incorporation of larger anions with more polarizable and lower electronegativity into the argyrodite lattice leads to larger lattice constant and weaker bonding. Fig. 6a shows the positive linear relationship between the lattice parameter and the anion size. However, despite the overall expansion of lattice with the increasing r_{anion}, E_a increases significantly (Fig. 6b). It is the reduction of BN_{inter} that hinders Li^+ conduction (Fig. 6c and 6d), and BN_{inter} is limited to the anion size on Wyckoff 4*a* site (Fig. 6e), which is consistent with recent reports [40,41]. Moreover, r_A is strongly negatively correlated with $Sconf_C$ (Fig. 6f), which may account for why site disorder controls the bottleneck of intercage conduction and affects the activation barriers for ionic conduction, as reported previously [42]. The underlying reason may be related to the rules of ion occupancy on Wyckoff 4*a* or Wyckoff 4*c* site (Table S3). Essentially, disorder on Wyckoff 4*c* or 4*d* site mainly arises from partial halogens substitution for X^- on Wyckoff 4*c* or 4*d* site, and larger halogens prefer to substitute for X^- on Wyckoff 4*a* site to generate larger r_A and smaller $Sconf_C$.

Therefore, the complex descriptors-E_a correlations can be simplified as follows: with the larger anion substitution, the lattice expands, while the bottleneck of the intercage conduction controlled by loss of site disorder narrows and then hinders the ionic conduction (Fig. 7).

3.4. *Promising compositions for cubic Li-argyrodite electrolytes*

The aforementioned results motivate us to design better Li-argyrodites by slightly decreasing the average anion radius. Promising compositions such as $Li_{6-x}PS_{5-x}Cl_{1+x}$ ($0<x<1$), $Li_{6+x}PS_{5+x}Br_{1-x}$

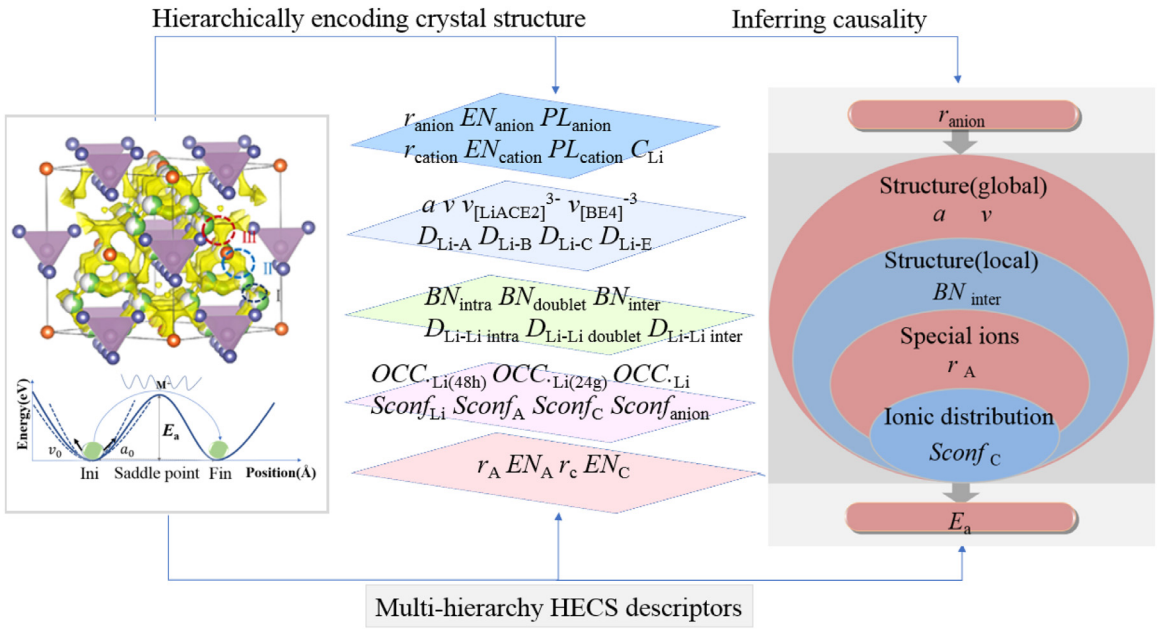

Fig. 7. Multi-hierarchy of the HECS descriptors for E_a in cubic Li-argyrodites and the simplified r_{anion}-descriptors-E_a correlation diagram (right). On the right, the variables in the same color regions (red or blue shades) exhibit positive correlation, whereas the variables in the different color regions have negative correlation.

($0<x<1$), $Li_6PS_5Cl_{0.5+x}Br_{0.5-x}$ ($0<x<0.5$), $Li_{6+x}PS_{5+x}Br_{0.75}I_{0.25-x}$ ($0<x<0.25$), and $Li_6PS_5Br_{0.75+x}I_{0.25-x}$ ($0<x<0.25$) are suggested and listed in Table S4. Among them, Li/P/S/Cl compositions have recently been studied experimentally [43,44]. In particular, $Li_{5.5}PS_{4.5}Cl_{1.5}$ exhibits a high Li^+ ion conductivity of 9.4 mS cm^{-1} at room temperature with activation energy of 0.29 eV, suggesting its excellent prospect as a solid electrolyte.

Furthermore, based on our above analysis, promising compositions can be generated by other means. Although Fig.S2a suggests that the cation size has minor direct influence on E_a, cation substitution can be used to modify the local disorder of the anions and in turn induce changes on the activation barrier. One successful example is the incorporation of Ge^{4+} with larger size than P^{5+} in Li_6PS_5I (Fig.S2a). With more Ge^{4+} substitution for P^{5+} in $Li_{6+x}P_{1-x}Ge_xS_5I$, an anion site disorder is induced and the activation energy reduces significantly, leading to an ionic conductivity reported so far of 5.4±0.8mS cm^{-1} in a cold-pressed state and 18.4±2.7mS cm^{-1} upon sintering [41].

Similarly, although Fig.S2b shows that the lithium content has minor direct influence on E_a, the analysis corresponds to the regime of uncorrelated ion conduction. Increasing the Li^+ content to a sufficiently high level may induce a change in the conduction mechanism towards highly correlated motion of Li^+, as demonstrated by recent studies [45-47], which can reduce the activation energy barrier significantly.

4. Conclusions

In summary, we introduce a paradigm of identifying descriptors linked to Li^+ conduction by hierarchically encoding the crystal structure and inferring their causalities *via* partial correlation analysis. Using cubic Li-argyrodites as an example, 32 HECS-descriptors are constructed and the smaller size anion substitution, especially on Wyckoff 4*a* site, is found to play a significant role in achieving lower activation energy, which results from the competing effects between the lattice space and bottleneck size controlled by framework site disorder. Based on this, promising compositions are suggested and $Li_{6-x}PS_{5-x}Cl_{1+x}$, especially $Li_{5.5}PS_{4.5}Cl_{1.5}$ (σ_{RT}=9.4mS cm^{-1}, E_a=0.29eV), have recently demonstrated very high Li^+ ion conductivity while the rest are novel compositions waiting for experimental validation. We believe that the unified representation power of the HECS-descriptor set will make it applicable in other types of SSE materials and promote relevant rational design for them.

Declaration of interests

The authors declare that they have no known competing financial interests or personal relationships that could have appeared to influence the work reported in this paper.

Author Statements

Qian Zhao contributed to the conceptualization, methodology, data curation and writing-original draft of the study. Liwen Zhang was responsible for ensuring the accuracy of E_a calculation by BVSE embedded in the SPSE platform. Bing He was the main developer of the SPSE platform. Anjiang Ye was the main developer of the CAVD software. Maxim Avdeev contributed to the writing-review & editing. Liquan Chen contributed to the management of the project. Siqi Shi contributed to the conceptualization, writing-review & editing and management of the project.

Declaration of Competing Interest

The authors declare that they have no known competing financial interests or personal relationships that could have appeared to influence the work reported in this paper.

Acknowledgments

This work was supported by the National Key Research and Development Program of China (No. 2017YFB0701600) and the National Natural Science Foundation of China (Nos. 11874254, 51622207, U1630134). All the computations were performed on the high performance computing platform provided by the High Performance Computing Center of Shanghai University.

Supplementary materials

Supplementary material associated with this article can be found, in the online version, at doi:10.1016/j.ensm.2021.05.033.

References

[1] H. Lee, P. Oh, J. Kim, H. Cha, S. Chae, S. Lee, J. Cho, Adv. Mater. 31 (2019) 1900376.
[2] X. Yu, L. Xue, J.B. Goodenough, A. Manthiram, Adv. Funct. Mater. (2020) 2002144, doi:10.1002/adfm.202002144.
[3] T. Ye, L. Li, Y. Zhang, Adv. Funct. Mater. (2020) 2000077, doi:10.1002/adfm.202000077.
[4] Q. Zhang, D. Cao, Y. Ma, A. Natan, P. Aurora, H. Zhu, Adv. Mater. 31 (2019) 1901131.
[5] L. Liang, X. Sun, J. Zhang, J Sun, L. Hou, Y. Liu, C. Yuan, Mater. Horiz. 6 (2019) 871–910.
[6] R. Chen, W. Qu, X. Guo, L. Li, F. Wu, Mater. Horiz. 3 (2016) 487–516.
[7] Y. Meesala, A. Jena, H. Chang, R.-S. Liu, ACS Energy Lett. 2 (2017) 2734–2751.
[8] A.R. Rodger, J. Kuwano, A.R. West, Solid State Ionics 15 (1985) 185–198.
[9] H. Yamane, S. Kikkawa, M. Koizumi, Solid State Ionics 25 (1987) 183–191.
[10] H.D. Lutz, P. Kuske, K. Wussow, Solid State Ionics 28 (1988) 1282–1286.
[11] O. Bohnke, C. Bohnke, J.L. Fourquet, Solid State Ionics 91 (1996) 21–31.
[12] A. Martinez-Juarez, C. Pecharromán, J.E. Iglesias, J.M. Rojo, J. Phys. Chem. B 102 (1998) 372–375.
[13] H.J. Deiseroth, S.T. Kong, H. Eckert, J. Vannahme, C. Reiner, T. Zaiss, M. Schlosser, Angew. Chem. Int. Edit. 47 (2008) 755–758.
[14] M. Matsuo, H. Oguchi, H. Maekawa, M. Ando, Y. Noda, T. Karahashi, S.I. Orimo, J. Am. Chem. Soc. 131 (2009) 894–895.
[15] K. Wakamura, Phys. Rev. B 56 (1997) 11593–11599.
[16] J.C. Bachman, S. Muy, A. Grimaud, H.H. Chang, N. Pour, S.F. Lux, O. Paschos, F. Maglia, S. Lupart, P. Lamp, L. Giordano, Y. Shao-Horn, Chem. Rev. 116 (2016) 140–162.
[17] Q. Zhao, L. Pan, Y.-J. Li, L.-Q. Chen, S.-Q. Shi, Rare Metals 37 (2018) 497–503.
[18] Y. Wang, W.D. Richards, S.P. Ong, L.J. Miara, J.C. Kim, Y. Mo, G. Ceder, Nature Mater. 14 (2015) 1026–1031.
[19] K. Fujimura, A. Seko, Y. Koyama, A. Kuwabara, I. Kishida, K. Shitara, C.A.J. Fisher, H. Moriwake, I. Tanaka, Adv. Energy Mater. 3 (2013) 980–985.
[20] A.D. Sendek, Q. Yang, E.D. Cubuk, K.-A.N. Duerloo, Y. Cui, E.J. Reed, Energy & Environ. Sci. 10 (2017) 306–320.
[21] H.-J. Deiseroth, J. Maier, K. Weichert, V. Nickel, S.-T. Kong, C. Reiner, Z. Anorg. Allg. Chem. 637 (2011) 1287–1294.
[22] M.A. Kraft, S.P. Culver, M. Calderon, F. Bocher, T. Krauskopf, A. Senyshyn, C. Dietrich, A. Zevalkink, J. Janek, W.G. Zeier, J. Am. Chem. Soc. 139 (2017) 10909–10918.
[23] B. He, S. Chi, A. Ye, P. Mi, L. Zhang, B. Pu, et al., Sci. Data 7 (2020) 151.
[24] S. Adams, Acta Cryst. B 57 (2001) 278–287.
[25] S. Adams, R.P. Rao, Phys. Status Solidi A 208 (2011) 1746–1753.
[26] K. Momma, F. Izumi, J. Appl. Crystallogr 44 (2011) 1272–1276.
[27] T.F. Willems, C.H. Rycroft, M. Kazi, J.C. Meza, M. Haranczyk, Microporous Mesoporous Mater. 149 (2012) 134–141.
[28] B. He, A. Ye, S. Chi, P. Mi, Y. Ran, L. Zhang, et al., Sci. Data 7 (2020) 153.
[29] R.D. Shannon, Acta Cryst. A 32 (1976) 751–767.
[30] N.D. Chatterjee, Applied Mineralogical Thermodynamics: Selected Topics, Springer Science & Business Media, 2013.
[31] E. Jones, T. Oliphant, P. Peterson, 2014, http://www. scipy. org.
[32] T.E. Oliphant, A Guide to NumPy, Trelgol, 2006.
[33] Hunter, Comput. Sci. Eng. 9 (2007) 90–95.
[34] Plotly, 2015, https://plot.ly.
[35] P.R. Rayavarapu, N. Sharma, V.K. Peterson, S. Adams, J. Solid State Electr. 16 (2011) 1807–1813.
[36] R.P. Rao, N. Sharma, V.K. Peterson, S. Adams, Solid State Ionics 230 (2013) 72–76.
[37] V. Epp, Ö. Gün, H.-J. Deiseroth, M. Wilkening, J. Phys.Chem. Lett. 4 (2013) 2118–2123.
[38] H. Wang, C. Yu, S. Ganapathy, E.R.-H. van Eck, L. van Eijck, M. Wagemaker, J. Power Sources 412 (2019) 29–36.
[39] N.J.J. de Klerk, I. Rosłoń, M. Wagemaker, Chem. Mater. 28 (2016) 7955–7963.
[40] Z. Wang, G. Shao, J. Mater. Chem. A 5 (2017) 21846–21857.
[41] M.A. Kraft, S. Ohno, T. Zinkevich, R. Koerver, S.P. Culver, T. Fuchs, A. Senyshyn, S. Indris, B.J. Morgan, W.G. Zeier, J. Am. Chem. Soc. 140 (2018) 16330–16339.
[42] T. Bernges, S.P. Culver, N. Minafra, R. Koerver, W.G. Zeier, Inorg. Chem. 57 (2018) 13920–13928.
[43] L. Zhou, K.-H. Park, X. Sun, F. Lalère, T. Adermann, P. Hartmann, L.F. Nazar, ACS Energy Lett. 4 (2018) 265–270.
[44] P. Adeli, J.D. Bazak, K.H. Park, I. Kochetkov, A. Huq, G.R. Goward, L.F. Nazar, Angew. Chem. Int. Ed. 58 (2019) 8681–8686.
[45] X. He, Y. Zhu, Y. Mo, Nature Commun. 8 (2017) 15893.
[46] Z. Zhang, Z. Zou, K. Kaup, R. Xiao, S. Shi, M. Avdeev, Y.S. Hu, D. Wang, B. He, H. Li, X. Huang, L.F. Nazar, L. Chen, Adv. Energy Mater. 9 (2019) 1902373.
[47] L. Zhou, A. Assoud, Q. Zhang, X. Wu, L.F. Nazar, J. Am. Chem. Soc. 141 (2019) 19002.

Supplemental information

Identifying descriptors for Li^+ conduction in cubic Li-argyrodites via hierarchically encoding crystal structure and inferring causality

Qian Zhao[a], Liwen Zhang[b], Bing He[c], Anjiang Ye[c],

Maxim Avdeev[d,e], Liquan Chen[a,f], Siqi Shi[a,b,*]

[a]*Materials Genome Institute, Shanghai University, Shanghai 200444, China*

[b]*School of Materials Science and Engineering, Shanghai University, Shanghai 200444, China*

[c]*School of Computer Engineering and Science, Shanghai University, Shanghai 200444, China*

[d]*Australian Nuclear Science and Technology Organization, New Illawarra Rd, Lucas Heights, NSW 2234, Australia*

[e]*School of Chemistry, The University of Sydney, Sydney 2006, Australia*

[f]*Key Laboratory for Renewable Energy, Institute of Physics, Chinese Academy of Sciences, Beijing 100190, China*

[*]Email: sqshi@shu.edu.cn (Siqi Shi)

Table S1. Values of the activation energy (E_a) for 50 cubic Li-argyrodite compounds obtained by experiments and BVSE software respectively. '\' indicates no corresponding experimental E_a value available from literatures.

NO.	Formula	E_a(eV) by experiments	E_a(eV) by BVSE
1	Li_7PS_6	0.334 [1]	0.283203
2	Li_7PSe_6	0.490 [2]	0.507813
3	Li_6PS_5Cl	0.201 [1], 0.382 [1], 0.440 [3], 0.295 [3], 0.451 [4]	0.322266
4	Li_6PS_5Br	0.1637 [1],0.5607 [1], 0.440 [1] 0.390 [3], 0.140 [3] 0.301 [4]	0.273438
5	$Li_6PS_5Cl_{0.5}Br_{0.5}$	0.310 [3], 0.144 [3], 0.368 [4]	0.332031
6	Li_6PS_5I	0.323 [1], 0.393 [1], 0.381 [4]	0.419922
7	Li_6AsS_5Br	\	0.263672
8	Li_6AsS_5I	\	0.371094
9	Li_6AsSe_5I	\	0.449219
10	$Li_{6.66}PSe_{5.66}Cl_{0.34}$	\	0.566406
11	$Li_{6.192}PS_{5.24}Br_{0.757}$	\	0.263672
12	$Li_{6.23}PSe_{5.23}I_{0.77}$	\	0.449219
13	$Li_6PS_5Cl_{0.75}Br_{0.25}$	0.409 [4]	0.322266
14	$Li_6PS_5Cl_{0.25}Br_{0.75}$	0.328 [4]	0.273438
15	$Li_6PS_{4.9}Se_{0.1}Br$	0.331 [5]	0.390625
16	$Li_6PS_{4.7}Se_{0.3}Br$	0.330 [5]	0.341797

17	$Li_6PS_{4.6}Se_{0.4}Br$	0.329 [5]	0.332031
18	$Li_6PS_{4.5}Se_{0.5}Br$	0.339 [5]	0.322266
19	$Li_6PS_{4.4}Se_{0.6}Br$	0.340 [5]	0.361328
20	$Li_6PS_{4.3}Se_{0.7}Br$	0.344 [5]	0.361328
21	$Li_6PS_{4.2}Se_{0.8}Br$	0.343 [5]	0.380859
22	$Li_6PS_{4.1}Se_{0.9}Br$	0.340 [5]	0.371094
23	Li_6PS_4SeBr	0.341 [5]	0.371094
24	$Li_6PS_5Br_{0.25}I_{0.75}$	0.350 [4]	0.351563
25	$Li_6PS_5Br_{0.75}I_{0.25}$	0.320 [4]	0.263672
26	$Li_6PS_5Br_{0.5}I_{0.5}$	0.310 [4]	0.312500
27	$Li_{6.1}P_{0.9}Ge_{0.1}S_5I$	0.386 [6]	0.390625
28	$Li_{6.15}P_{0.85}Ge_{0.15}S_5I$	0.362 [6]	0.380859
29	$Li_{6.2}P_{0.8}Ge_{0.2}S_5I$	0.360 [6]	0.380859
30	$Li_{6.25}P_{0.75}Ge_{0.25}S_5I$	0.306 [6], 0.21 [6]	0.371094
31	$Li_{6.3}P_{0.7}Ge_{0.3}S_5I$	0.269 [6]	0.371094
32	$Li_{6.4}P_{0.6}Ge_{0.4}S_5I$	0.240 [6]	0.361328
33	$Li_{6.5}P_{0.5}Ge_{0.5}S_5I$	0.239 [6]	0.332031
34	$Li_{6.6}P_{0.4}Ge_{0.6}S_5I$	0.238 [6], 0.16 [6]	0.341797
35	$Li_{6.7}P_{0.3}Ge_{0.7}S_5I$	0.237 [6]	0.322266
36	$Li_{6.8}P_{0.2}Ge_{0.8}S_5I$	0.237 [6]	0.312500
37	$Li_{6.9}P_{0.1}Ge_{0.9}S5I$	0.248 [6]	0.322266
38	$Li_{6.025}P_{0.975}Si_{0.025}S_5Br$	0.192 [7]	0.273438
39	$Li_{6.05}P_{0.95}Si_{0.05}S_5Br$	0.172 [7]	0.273438
40	$Li_{6.075}P_{0.925}Si_{0.075}S_5Br$	0.175 [7]	0.283203
41	$Li_{6.10}P_{0.90}Si_{0.10}S_5Br$	0.221 [7]	0.253906
42	$Li_{6.125}P_{0.875}Si_{0.125}S_5Br$	0.171 [7]	0.263672
43	$Li_{6.15}P_{0.85}Si_{0.15}S_5Br$	0.188 [7]	0.263672
44	$Li_{6.175}P_{0.825}Si_{0.175}S_5Br$	0.142 [7]	0.273438
45	$Li_{6.20}P_{0.80}Si_{0.20}S_5Br$	0.250 [7]	0.263672
46	$Li_{6.225}P_{0.775}Si_{0.225}S_5Br$	0.245 [7]	0.263672
47	$Li_{6.25}P_{0.75}Si_{0.25}S_5Br$	0.221 [7]	0.263672
48	$Li_{6.30}P_{0.70}Si_{0.30}S_5Br$	0.238 [7]	0.244141
49	$Li_{6.35}P_{0.65}Si_{0.35}S_5Br$	0.242 [7]	0.253906
50	$Li_{6.50}P_{0.50}Si_{0.50}S_5Br$	0.267 [7]	0.253906

Table S2. 32 HECS-descriptors with their corresponding descriptions and formulas.

Descriptors	**Descriptions and formulas**
r_{cation}, r_{anion}, r_A, r_C	Average ionic radius (r) for the cations M^{5+} and N^{4+}, the anions $Y(1)^{2-}$, $Y(2)^{2-}$ and X^-, the mixed ions ($Y(2)^{2-}$ and X^-)

	on Wyckoff 4*a* site and Wyckoff 4*c* or 4*d* site, given by the following expressions: $r_{cation} = (1-y)r_M + yr_N$; (1) $r_{anion} = \frac{4r_{Y(1)}+(2-x)r_{Y(2)}+xr_X}{6}$; (2) $r_A, r_C = Occ._{.Y(2)}\, r_{Y(2)} + Occ._X\, r_X$; (3) Occ. symbolizes site occupancy.
$\boldsymbol{C}_{\mathbf{Li}}$	Lithium content
$\boldsymbol{EN}_{\mathbf{cation}}$, $\boldsymbol{EN}_{\mathbf{anion}}$, $\boldsymbol{EN}_{\mathbf{A}}$, $\boldsymbol{EN}_{\mathbf{C}}$	Average Pauling electronegativity (*EN*) for the cations M^{5+} and N^{4+}, the anions $Y(1)^{2-}$, $Y(2)^{2-}$ and X^-, the mixed ions ($Y(2)^{2-}$ and X^-) on Wyckoff 4*a* site and Wyckoff 4*c* or 4*d* site[8]. $EN_{cation} = (1-y)EN_M + yEN_N$; (4) $EN_{anion} = \frac{4EN_{Y(1)} + (2-x)EN_{Y(2)} + xEN_X}{6}$; (5) $\mathrm{EN}_A, EN_C = EN_O -$ $\sqrt{Occ._{.Y(2)}\left(EN_{Y(2)} - EN_O\right)^2 + Occ._X\,(EN_X - EN_O)^2}$;(6)
$\boldsymbol{PL}_{\mathbf{cation}}$, $\boldsymbol{PL}_{\mathbf{anion}}$	Average ionic polarizability (*PL*) for the cations M^{5+} and N^{4+}, the anions $Y(1)^{2-}$, $Y(2)^{2-}$ and X^-. $PL_{cation} = (1-y)PL_M + yPL_N$; (7) $PL_{anion} = \frac{4PL_{Y(1)} + (2-x)PL_{Y(2)} + xPL_X}{6}$; (8)
$\boldsymbol{Occ.Li}_{\boldsymbol{(48h)}}$, $\boldsymbol{Occ.Li}_{\boldsymbol{(24g)}}$, ***Occ.Li***	Lithium ion occupancy on Wyckoff 48*h* site, Wyckoff 24*g* site, and all site respectively.

$\boldsymbol{Sconf}_{\mathbf{Li}}$, $\boldsymbol{Sconf}_{\mathbf{anion}}$, $\boldsymbol{Sconf}_{\mathbf{A}}$, $\boldsymbol{Sconf}_{\mathbf{C}}$	configurational entropy (*Sconf*) for the mobile Lithium ions, all the anions ($Y(1)^{2-}$, $Y(2)^{2-}$ and X^{-}), the mixed ions ($Y(2)^{2-}$ and X^{-}) on Wyckoff 4*a* site and Wyckoff 4*c* or 4*d* site ,calculated by $$S_{conf} = -R \sum_j q_j \ \sum_i X_{ij} \ lnX_{ij}. \quad (9)$$ Where q_j is the total number of sites in the sublattice j, X_{ij} is the mole fraction (occupancy) of the ion i on the j-th sublattice
$\boldsymbol{a}$	lattice parameter
$\boldsymbol{V}$	unit cell volume
$\boldsymbol{V}_{[BE_4]^{3-}}$, $\boldsymbol{V}_{[LiACE_2]^{3-}}$	Volume (V) for tetrahedra $[BE_4]^{3-}$, Frank−Kasper polyhedral $[LiACE_2]^{3-}$ respectively.
$\boldsymbol{D}_{\mathbf{Li\text{-}A}}$, $\boldsymbol{D}_{\mathbf{Li\text{-}B}}$, $\boldsymbol{D}_{\mathbf{Li\text{-}C}}$, $\boldsymbol{D}_{\mathbf{Li\text{-}E}}$	interatomic distance (D) between Li and nearest neighboring ions on Wyckoff 4*a*, 4*b*, 4*c* or 4*d* and 16*e* site respectively.
$\boldsymbol{D}_{\mathbf{Li\text{-}Li\ intra}}$, $\boldsymbol{D}_{\mathbf{Li\text{-}Li\ doublet}}$, $\boldsymbol{D}_{\mathbf{Li\text{-}Li\ inter}}$	interatomic distance (D) between Li and nearest neighboring Li on the intra-cage, doublet and inter-cage pathway respectively.
$\boldsymbol{BN}_{\mathbf{intra}}$, $\boldsymbol{BN}_{\mathbf{doublet}}$, $\boldsymbol{BN}_{\mathbf{inter}}$	bottleneck size (BN) for the intra-cage, doublet and inter-cage pathway respectively.

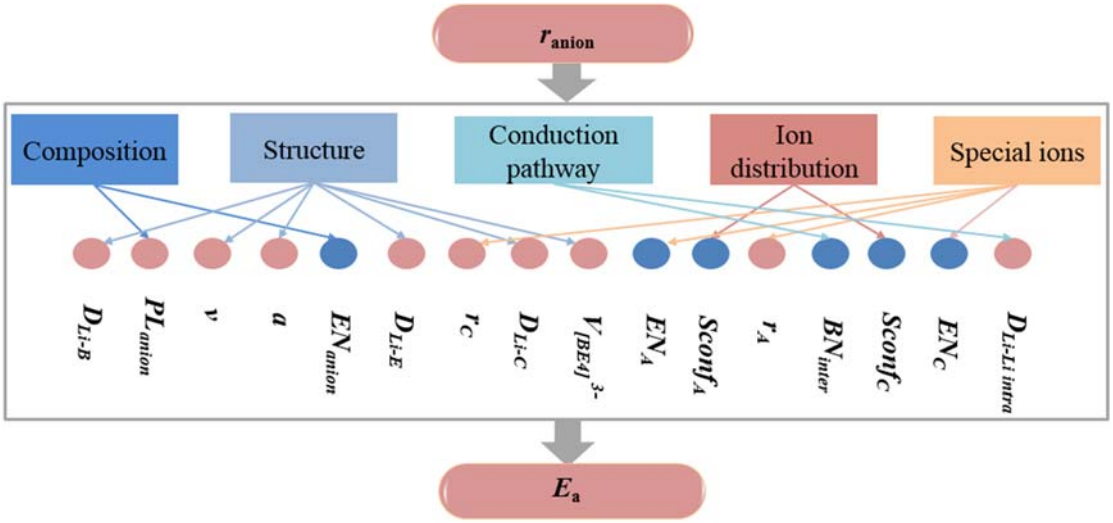

Fig. S1. r_{anion}-descriptors-E_a correlation network. Descriptors listed in the middle belong to five categories respectively and are significantly correlated with both r_{anion} and E_a, arranging from left to right according to the strength of the descriptors-Ea correlation. Among them, descriptors labeled with blue (red) balls are negatively (positively) correlated with both E_a and r_{anion}.

Table S3. Reported anion occupation at the Wyckoff 4*a* and 4*c* (or 4*d*) site respectively for 50 cubic Li-argyrodite structures.

NO.	Formula	Wyckoff 4*c* or 4*d* site	Wyckoff 4*a* site	Ref.
1	Li_7PS_6	S	S	[9]
2	Li_7PSe_6	Se	Se	[9]
3	Li_6PS_5Cl	0.615Cl, 0.385S	0.385Cl, 0.615S	[4]
4	Li_6PS_5Br	0.221Br, 0.779S	0.221S, 0.779Br	[4]
5	$Li_6PS_5Cl_{0.5}Br_{0.5}$	0.211Cl, 0.297Br, 0.492S	0.289Cl, 0.203Br, 0.508S	[4]
6	Li_6PS_5I	S	I	[4]

7	Li_6AsS_5Br	0.930S, 0.07Br	0.916Br、0.084S	[10]
8	Li_6AsS_5I	S	I	[10]
9	Li_6AsSe_5I	Se	I	[10]
10	$Li_{6.66}PSe_{5.66}Cl_{0.34}$	0.834Se, 0.167Cl	0.827 Se, 0.171Cl	[10]
11	$Li_{6.192}PS_{5.24}Br_{0.757}$	0.842S, 0.157Br	0.398S, 0.600Br	[11]
12	$Li_{6.23}PSe_{5.23}I_{0.77}$	Se	0.229 Se, 0.770 I	[10]
13	$Li_6PS_5Cl_{0.75}Br_{0.25}$	0.435Cl, 0.148Br, 0.418S	0.315Cl, 0.102Br,0.582S	[4]
14	$Li_6PS_5Cl_{0.25}Br_{0.75}$	0.140Cl, 0.156Br, 0.705S	0.111Cl,0.595Br,0.296S	[4]
15	$Li_6PS_{4.9}Se_{0.1}Br$	0.209Br, 0.692S, 0.100Se	0.792Br, 0.209S	[5]
16	$Li_6PS_{4.7}Se_{0.3}Br$	0.825S, 0.175Se	Br	[5]
17	$Li_6PS_{4.6}Se_{0.4}Br$	0.730S, 0.272Se	Br	[5]
18	$Li_6PS_{4.5}Se_{0.5}Br$	0.638S, 0.364Se	Br	[5]
19	$Li_6PS_{4.4}Se_{0.6}Br$	0.569S, 0.433Se	Br	[5]
20	$Li_6PS_{4.3}Se_{0.7}Br$	0.583S, 0.419Se	Br	[5]
21	$Li_6PS_{4.2}Se_{0.8}Br$	0.519S, 0.483Se	Br	[5]
22	$Li_6PS_{4.1}Se_{0.9}Br$	0.516S, 0.486Se	Br	[5]
23	Li_6PS_4SeBr	0.504S, 0.496Se	Br	[5]
24	$Li_6PS_5Br_{0.25}I_{0.75}$	0.007Br, 0.009I, 0.985S	0.243Br, 0.741I, 0.015S	[4]
25	$Li_6PS_5Br_{0.75}I_{0.25}$	0.087Br, 0.069I, 0.845S	0.663Br, 0.181I, 0.155S	[4]

26	$Li_6PS_5Br_{0.5}I_{0.5}$	0.015Br, 0.965S, 0.020I	0.485Br, 0.035S, 0.48I	[4]
27	$Li_{6.1}P_{0.9}Ge_{0.1}S_5I$	0.007I, 1.007S	1.0006I, 0.0006S	[6]
28	$Li_{6.15}P_{0.85}Ge_{0.15}S_5I$	0.0005I, 1.0005S	1.0005I, 0.0005S	[6]
29	$Li_{6.2}P_{0.8}Ge_{0.2}S_5I$	0.0207I, 0.9807S	0.9807I, 0.0207S	[6]
30	$Li_{6.25}P_{0.75}Ge_{0.25}S_5I$	0.0146I, 0.9866S	0.9866I, 0.0146S	[6]
31	$Li_{6.3}P_{0.7}Ge_{0.3}S_5I$	0.0106I, 0.9906S	0.9906I, 0.0106S	[6]
32	$Li_{6.4}P_{0.6}Ge_{0.4}S_5I$	0.0105I, 0.9905S	0.9905I, 0.0105S	[6]
33	$Li_{6.5}P_{0.5}Ge_{0.5}S_5I$	0.9686S, 0.0326I	0.9686I, 0.0326S	[6]
34	$Li_{6.6}P_{0.4}Ge_{0.6}S_5I$	0.9696S, 0.0316I	0.9696I, 0.0316S	[6]
35	$Li_{6.7}P_{0.3}Ge_{0.7}S_5I$	0.9447S, 0.0567I	0.9447I, 0.0567S	[6]
36	$Li_{6.8}P_{0.2}Ge_{0.8}S_5I$	0.92713S, 0.07313I	0.92713I, 0.07313S	[6]
37	$Li_{6.9}P_{0.1}Ge_{0.9}S5I$	0.878S, 0.138I	0.878I, 0.138S	[6]
38	$Li_{6.025}P_{0.975}Si_{0.025}S_5Br$	0.801S, 0.201Br	0.801Br, 0.201S	[7]
39	$Li_{6.05}P_{0.95}Si_{0.05}S_5Br$	0.791S, 0.211Br	0.791Br, 0.211S	[7]
40	$Li_{6.075}P_{0.925}Si_{0.075}S_5Br$	0.771S, 0.231Br	0.771 Br, 0.231 S	[7]
41	$Li_{6.10}P_{0.90}Si_{0.10}S_5Br$	0.791 S, 0.211Br	0.791Br, 0.211 S	[7]
42	$Li_{6.125}P_{0.875}Si_{0.125}S_5Br$	0.821S, 0.181Br	0.821Br, 0.181 S	[7]
43	$Li_{6.15}P_{0.85}Si_{0.15}S_5Br$	0.841S, 0.161Br	0.841Br, 0.161 S	[7]
44	$Li_{6.175}P_{0.825}Si_{0.175}S_5Br$	0.791S, 0.211Br	0.791Br, 0.211S	[7]
45	$Li_{6.20}P_{0.80}Si_{0.20}S_5Br$	0.791S, 0.211Br	0.791Br, 0.211S	[7]
46	$Li_{6.225}P_{0.775}Si_{0.225}S_5Br$	0.831 S, 0.171Br	0.831 Br, 0.171S	[7]
47	$Li_{6.25}P_{0.75}Si_{0.25}S_5Br$	0.841 S, 0.161Br	0.84 Br, 0.161S	[7]
48	$Li_{6.30}P_{0.70}Si_{0.30}S_5Br$	0.821S, 0.181Br	0.821 Br, 0.181S	[7]

49	$Li_{6.35}P_{0.65}Si_{0.35}S_5Br$	0.831 S, 0.171Br	0.831Br, 0.171S	[7]
50	$Li_{6.50}P_{0.50}Si_{0.50}S_5Br$	0.821S, 0.181Br	0.821Br, 0.181S	[7]

Table S4. Selected promising compositions and their average anion size (r_{anion}).

Compositions	Formula	r_{anion} (Å)
$Li_{6-x}PS_{5-x}Cl_{1+x}$		
x=0	Li_6PS_5Cl	1.835
x=0.125	$Li_{5.875}PS_{4.875}Cl_{1.125}$	1.8343
x=0.25	$Li_{5.75}PS_{4.75}Cl_{1.25}$	1.83375
x=0.375	$Li_{5.625}PS_{4.625}Cl_{1.375}$	1.833125
x=0.5	$Li_{5.5}PS_{4.5}Cl_{1.5}$	1.8325
x=0.55	$Li_{5.45}PS_{4.45}Cl_{1.55}$	1.83225
x=0.6	$Li_{5.4}PS_{4.4}Cl_{1.6}$	1.832
$Li_{6+x}PS_{5+x}Br_{1-x}$		
x=0	Li_6PS_5Br	1.86
x=0.125	$Li_{6.125}PS_{5.125}Br_{0.875}$	1.8575
x=0.25	$Li_{6.25}PS_{5.25}Br_{0.75}$	1.855
x=0.375	$Li_{6.375}PS_{5.375}Br_{0.625}$	1.8525
x=0.5	$Li_{6.5}PS_{5.5}Br_{0.5}$	1.85
$Li_6PS_5Cl_{0.5+x}Br_{0.5-x}$		
x=0	$Li_6PS_5Cl_{0.5}Br_{0.5}$	1.8475
x=0.125	$Li_6PS_5Cl_{0.625}Br_{0.375}$	1.844375
x=0.25	$Li_6PS_5Cl_{0.75}Br_{0.25}$	1.84125

x=0.375	$Li_6PS_5Cl_{0.85}Br_{0.125}$	1.83058
$Li_{6+x}PS_{5+x}Br_{0.75}I_{0.25-x}$		
x=0	$Li_6PS_5Br_{0.75}I_{0.25}$	1.87
x=0.125	$Li_{6.125}PS_{5.125}Br_{0.75}I_{0.125}$	1.8625
$Li_6PS_5Br_{0.75+x}I_{0.25-x}$		
x=0.125	$Li_6PS_5Br_{0.825}I_{0.125}$	1.84867

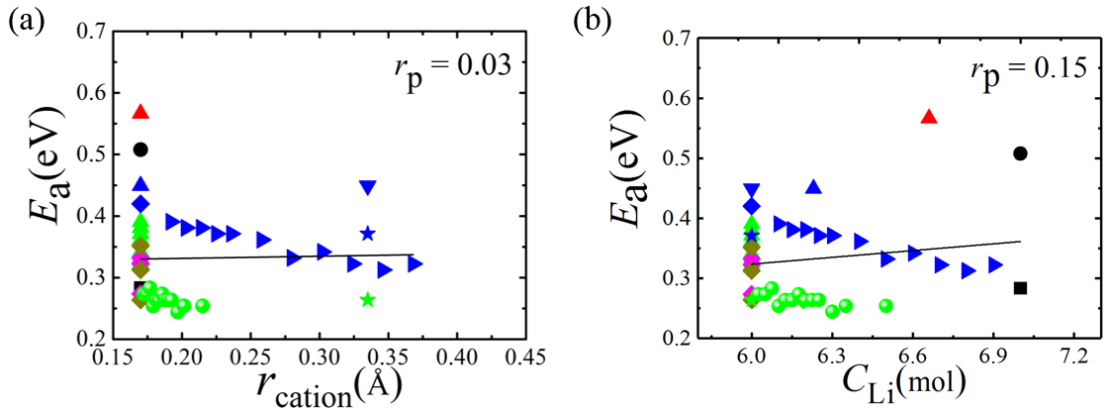

Fig. S2. Scatter diagram of (a) r_{cation}-E_a linear correlation, (b) C_{Li} -E_a linear correlation. The best-fit linear regression lines (black straight line) together with the Pearson's correlation coefficients r_p (in the top-right corner) are displayed in each panel.

References

[1] H.-J. Deiseroth, J. Maier, K. Weichert, V. Nickel, S.-T. Kong, C. Reiner, *Z. Anorg. Allg. Chem.*, 2011, **637**, 1287-1294.

[2] H.M. Chen, C. Maohua, S. Adams, *Phys. Chem. Chem. Phys.*, 2015, **17**, 16494-16506.

[3] H. Wang, C. Yu, S. Ganapathy, E.R.H. van Eck, L. van Eijck, M. Wagemaker, *J. Power Sources*, 2019, **412**, 29-36.

[4] M.A. Kraft, S.P. Culver, M. Calderon, F. Bocher, T. Krauskopf, A. Senyshyn, C. Dietrich, A. Zevalkink, J. Janek, W.G. Zeier, *J. Am. Chem. Soc.*, 2017, **139**, 10909-

10918.
[5] T. Bernges, S.P. Culver, N. Minafra, R. Koerver, W.G. Zeier, *Inorg. Chem.*, 2018, **57**, 13920-13928.
[6] M.A. Kraft, S. Ohno, T. Zinkevich, R. Koerver, S.P. Culver, T. Fuchs, A. Senyshyn, S. Indris, B.J. Morgan, W.G. Zeier, *J. Am. Chem. Soc.*, 2018, **140**, 16330-16339.
[7] N. Minafra, S.P. Culver, T. Krauskopf, A. Senyshyn, W.G. Zeier, *J. Mater. Chem. A*, 2018, **6**, 645-651.
[8] W. Ye, C. Chen, Z. Wang, I.H. Chu, S.P. Ong, *Nature Commun.*, 2018, **9**, 3800.
[9] S.T. Kong, Ö. Gün, H, B. Koch, H.J. Deiseroth, H. Eckert, C. Reiner, *Chem.-Eur. J*. 2010, 16, 5138-5147.
[10] S.T. Kong, H.J. Deiseroth, C. Reiner, Ö. Gün, E. Neumann, C. Ritter, D. Zahn, *Chem.-Eur. J.*, 2010, 16, 2198-2206.
[11] H.J. Deiseroth, S.T. Kong, H. Eckert, J. Vannahme, C. Reiner, T. Zaiss, M. Schlosser, *Angew. Chem. Int. Ed.*, 2008, 47, 755-758.